Int. J. Electrochem. Sci., 14 **(2019)** 8949 – 8972, doi: 10.20964/2019.09.46

International Journal of ELECTROCHEMICAL SCIENCE
www.electrochemsci.org

Electrochemical and surface studies of 0.95 Mg-Al-alloy and pure copper joints prepared using friction stir welding with low-medium-high tool travel speeds

Neetesh Soni, Yang Yaocheng, Adepu Kumar, Yin Caihong, Liu Li, Ambrish Singh[*], *Yuanhua lin*

1 School of Materials Science and Engineering, Southwest Petroleum University, 8 Xindu district-610500, Chengdu city, Sichuan province, China.
2 Department of Mechanical Engineering, National Institute of Technology , Warangal, India
[*]E-mail: vishisingh4uall@gmail.com; drambrishsingh@gmail.com

Received: 2 April 2019 / *Accepted:* 2 July 2019 / *Published:* 31 July 2019

Friction stir welding (FSW) is a technique currently used by weldment industries. In this study, FSW was used to join two dissimilar metals, copper and 0.95 Mg-Al-alloy. The process parameters and tool travelling speed were determined for a defect-free weldment. The corrosion resistance of the joint was studied with electrochemical methods in 3.5 wt.% NaCl solution. A scanning Kelvin probe was used to detect localized changes at the metal and weldment surface. Samples were characterized to explore the metallurgical effects and the effect of process parameters on the microstructure during the welding deformation process. The primary α-Al phase formed during solidification can significantly limit the growth of the Cu_9Al_4 phase as observed by optical microscopy. With the increase in tool travel speed, α-Al precipitates in the CuAl matrix created during welding became coarser. The electrochemical results illustrate that the tool travelling speed of 40 mm/min produced the greatest corrosion resistant property.

Keywords: Friction Stir-Welding; Scanning kelvin probe; Aluminum-Copper; Corrosion; Polarization; Tool travel speed.

1. INTRODUCTION

Friction stir welding is an emerging method to join dissimilar metals [1]. Dissimilar joints, such as aluminum-copper, Al-steel, and Al-magnesium, have recently been of interest because of their demand. Industries are more focused on these types of joints due to enhanced durability, reduced weight percentage of materials, and cost effectiveness. In the last two decades, 0.95 Mg-Al-alloy and copper dissimilar joints have become the backbone of these industries. These joints are mostly as an electric coupler in aircraft, the oil and gas industries, in high speed trains in a heat exchanger, in an electrical heavy load (power) supply and as connectors of hydraulic pistons. Per a report by IACS (International

Annealed Copper Standard), copper shows a better conductivity (100%) behind silver (105%). Copper is very expensive compared to aluminum, and aluminum alloys have good conductivity (61%) behind gold (71%) [2]. Therefore, achieving 61% conductivity is the main motivation to use 0.95 Mg-Al-alloy. An 0.95 Mg-Al-alloy and pure copper bimetallic joint is inexpensive and therefore saves enormous cost for industries. The joint has high strength, high workability, and good corrosion resistance [3]. The dissimilar joint fabricated by FSW of aluminum-copper avoids the inhomogeneity of microstructural properties, produces higher mechanical properties and fulfills the performance parameters of electrochemical properties compared with other welding techniques [4]. During FSW, the formation of intermetallic precipitate and its distribution along the weldment matrix enhances the galvanic corrosion. The reduction in the grain size in the weldment region influences the rate of corrosion [5].

Considering a previous study [6], the effect of the generated temperature and microstructural assessment of the FSW of 0.95 Mg-Al-alloy to copper was analyzed. Some intermetallic compounds formed were identified during welding, such as $CuAl_2$, CuAl, and Cu_9Al_4, with small quantities of α-Al and a saturated solid solution (SSS) of aluminum in copper. The prominent temperature observed in the weld zone was approximately 580 °C. Investigation of the low, medium, and high rotational speeds with the respective feed rate illustrated that a medium tool rotational rate and 30 mm/min tool traverse speed provides better microstructural and mechanical properties than the other parameters [7]. Enhancing the travelling speed of the tool decreases the grain structures of the weld zone, which can be observed by comparing the XRD patterns of the base metals and welded samples [8]. Fabrication of the friction stir welding of aluminum-copper generates internal residual stress (IRS) in the dynamic recrystallized zone (DXZ) causing modifications to the electrochemical and mechanical properties of the weldment [9-11]. This is influenced by the process parameters of the machine setup and is also affected by the composition of the base materials [10] identified in the region where corrosion occurs. 2024-T3-Al alloys joined by friction stir welding were examined in a corrosion study, concluding that the corrosion rate in DXZ was greater than that in the base material (BM) and the thermomechanical affected-zone (TMA-Zone) because of the formation of intermetallic compounds from elements present in the alloys [11]. Previous research of 2024-T351-Al alloys in a 0.1 M NaCl solution demonstrated the corrosion properties were dependent on the travel speed and rotational speed of tools [12]. Moreover, in the dynamic recrystallized zone the attack by intergranular corrosion is high at a very low tool speed rotation (215 rpm) compared to the thermo-mechanical affected-zone and base metal. Corrosion due to the faster rotational speed of the tool during friction stir-welding and the feasibility for the absence of enhanced corrosion resistance due to the lack of the Al_2Cu phase in the DXZ were investigated [13]. The corrosion resistance in the weldment region of DXZ is better in an alkaline solution, and selection of a faster tool rotational speed during FSW enhances the fabrication of a 2219-O-Al alloy joint [14]. The tool pin profile also affects the corrosion resistance properties and the generation of heat influences the corrosion resistance of the 2219-Al alloy [15]. The elevated temperature due to heat generation is useful in preventing thse formation of Al_2Cu particles and enhancing the corrosion resistance.

Aluminum and copper are dissimilar metals, although they show great interactions with each other at temperatures greater than 120°C, forming a brittle intermetallic at their joined interface. Very few researchers have focused on aluminum-copper for electrochemical investigation. The available data for the research on FSW of unlike metals does not include a methodical study to characterize the

microstructural formation. The properties of dissimilar welds, effects of temperature, material flow and interaction are also not well reported or discussed. In the current work, a feasibility study of joining 0.95 Mg-Al-alloys to pure copper plates 3-mm thick by FSW was performed. A systematic study was conducted to analyze the weldment made from the 0.95 Mg-Al-alloy with pure Cu joints using FSW, a X-ray diffraction (XRD) study, microhardness testing and scanning electron microscopy (SEM).

2. EXPERIMENT

2.1. Selection of materials with elemental analysis

Sheets with a thickness of 3 mm were used for the 0.95 Mg-Al-alloy and pure copper to perform the material elemental analyses. The study was performed using the Materials Development Division/ Standard Operating Procedure for copper alloys (MDD/SOP/Cu) and optical emission spectrometer/model DV6 (OES/DV-6) for the 0.95 Mg-Al-alloy test method following the ASTM/E1251 standard. All of the material elemental analyses were performed at the Defense Research and Development Laboratory/Chemistry/Materials Development Division (DRDL/CHEM/MDD) in Hyderabad. The results as represented in Table 1. Due to the limitation of the test material, pure copper and 0.95 Mg-Al-alloy plates of 260 × 60 × 3 mm in size were used in the form of rolled plates.

Table 1. Chemical composition of the base metals (Wt. %).

Pure Copper	Zn	Al	Si	Sn	P	S	Pb	Fe	Cu
	0.005	0.005	0.005	0.007	0.001	0.013	0.01	0.04	Bal.99.9
0.95 Mg-Al-alloy	Cu	Zn	Si	Ti	Mg	Mn	Cr	Fe	Al
	0.2	0.013	0.07	0.02	1.0	0.11	0.12	0.3	Bal. 98.2

2.2. Selection of the tool materials with chemical composition

Welding with the friction stir joining approach requires the procedure parameters and work piece be adjusted with the machine setup and fixtures. The 260 × 60 × 3 mm samples were fixed, and the intended welding surface cleaned using a piece of cotton gouge soaked in acetone. This cleaning step is necessary to avoid contamination by impurities in the weld beads. The tilt angle was 2° and the tool revolving speed was 1350 rpm. The work pieces were oriented with copper on the advancing side and aluminum on the retreating side because of the heat dissipation when joining two different materials.

AISI-H13 tool steel was used as the tool material for its good strength and hardness at elevated temperature, wear resistance, suitable toughness, thermal fatigue strength, heat cracking resistance,

machinability, availability, and cost. The typical chemical composition of AISI-H13 tool steel is presented in Table 2.

Table 2. Chemical composition of AISI-H13 tool steel (Wt. %).

Element	C	Mn	P	S	Si	Cr	V	Mo
Amount (Wt. %)	0.4	0.3	0.02	0.003	1	5.2	1.0	1.5

AISI-H13 tools were made with a 24 mm shoulder and 20 mm collet diameter with tapered threaded pin profile (Ø6 mm, 2.7 mm length). The rotation of the tools was 1350 rpm angled at 2° with a fixed traveling speed of 30, 40, and 50 mm/min.

2.3. Sample preparation and mounting

An area of 1.5 × 1.5 cm was cut from the welded sample that contained the Al-HAZ-TMAZ-DXZ-TMAZ-HAZ-Cu zones. The samples were mechanically abraded using 120 to 600 grit SiC papers and were polished using diamond paste. After polishing, etching was performed using two different etchants for copper (distilled water-100 ml, HCl-15 ml, and ferric chloride-2.5 g) and three for the 0.95 Mg-Al-alloy (HF-2 ml, HCl-3 ml, HNO_3-5 ml, distilled water-190 ml). The samples were then used for the microstructural property studies and corrosion tests. Prior to corrosion, the area was studied using XRD-Cu-K_α radiation, optical microscopy and SEM.

2.4. Micrography examination

The microstructures of the samples were studied using a Leitz optical microscope. Huvitz upright HRM-300 Series microscope was used to study the weldment structure of the cross-section region. Specimens of 30 × 3 mm in size were cut from the middle of the samples for the microhardness analysis.

2.5. Microhardness analysis

The test was performed using a Vickers digital microhardness tester (Model: Autograph, Make: Shimatzu) with a 200 g load for a period of 15 seconds. The pattern for microhardness using the Vickers digital machine is shown in Figure 1. The microhardness was tested at intervals of 0.15 mm across the unaffected BM, processed zone, TMA-Zone, and heat affected zone (HAZ).

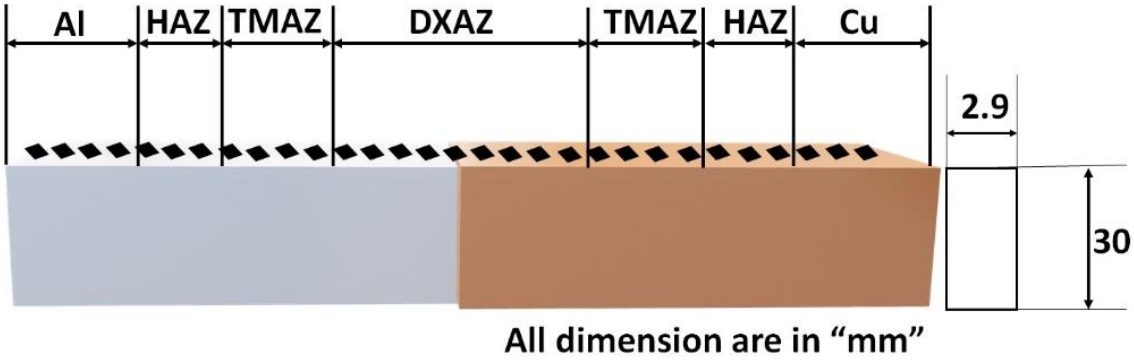

Figure 1. Pattern followed for the microhardness test using a Vickers digital machine.

2.6. XRD examination of the welded samples

The phase analysis of the 0.95 Mg-Al-alloy and pure copper welded samples were carried out by the X-ray diffraction technique. The diffraction spectra obtained via the XRD technique were examined using the PANalytical X'pert Highscore plus software. The peak shift was determined for 0.95 Mg-Al-alloy and pure Cu metal at the scan range of 10° to 120° angle with scan step is 0.01 to accurately identify peaks on the welded surfaces.

2.7. Electrochemical analyses

Electrochemical examinations of the specimens were performed at room temperature in 3.5 wt.% NaCl solution. The bare surface of the interface area in the corrosive solution was 1.5 cm^2. The impedance and polarization experiments were conducted using an Autolab workstation.

The tests were conducted in an assembly of three electrode cells according to ASTM: G69 using a saturated calomel electrode (SCE) as the reference electrode, a corrosive electrolyte (60 g/L NaCl) and an aluminum-copper sample with dimensions of 2.8 × 15 × 15 mm as the working electrode. The experiments were repeated several times to ensure reproducibility of the results.

The potentiodynamic tests were performed from -2.5 V to 2.5 V at a scan rate of 1 mV/s. Before the experiment, an immersion period of 30 minutes was provided for a reproducible homogeneous surface condition with a stable corrosion potential.

Scanning Kelvin probe (SKP) tests were conducted on Princeton equipment using the Versa scan software. The potential at the electrode surface was recorded before and after immersing in the corrosive media. The cross-section potential was also recorded to provide additional value to the obtained parameters.

3. RESULTS AND DISCUSSION

The joint of dissimilar metals (0.95 Mg-Al-alloy and pure copper) made by FSW enhances the corrosion resistance properties and a key role is played by the tools travel speeds during weldment, such as 30, 40, and 50 mm/min. The joint reflects the different morphologies of the surface as shown in Figure

2. The full-welded images of 0.95 Mg-Al Alloy and pure copper samples after various tools travel speed (a) 30, (b) 40, and (c) 50 mm/min are shown, respectively. As shown in Figure 2(a), the surface morphology prepared using a 30 mm/min tool travel speed was acceptable because no surface defects were detected. As shown in Figure 2(b), the surface prepared using a 40 mm/min tool travel speed was much better than the other surfaces because there was lack of surface roughness and very smooth concentric rings are formed throughout the FSW. The welded sample in Figure 2(b) shows the lack of flash generation and surface defects. Figure 2(c) shows some micro voids on the surface that were clearly visible during visual examination of the welded samples. The voids on the surface proves that this weldment of the sample prepared at a 50 mm/min tool travel speed was not better than the others.

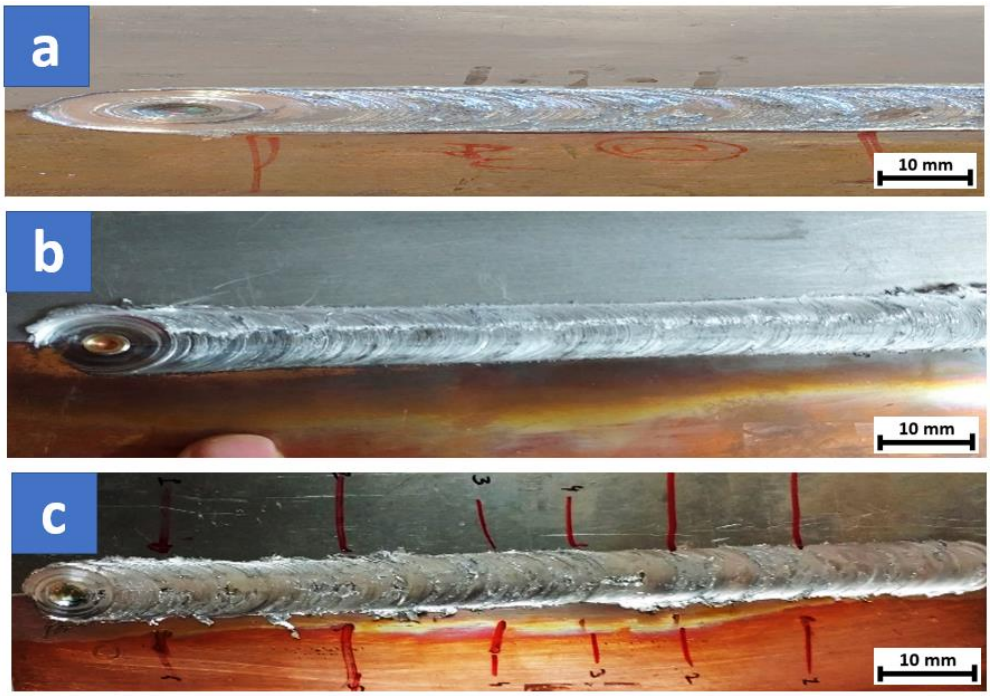

Figure 2. Surface morphology of the full-welded zones of 0.95 Mg-Al-alloys and pure copper samples prepared by (a) 30, (b) 40, and (c) 50 mm/min tool travel speeds.

3.1. Macrography observation

The weldments were without surface defects and had an even appearance, as shown in Figure 3. There was no flash formation during welding. The macrostructures and microstructures in the DXZ zone formed at 30, 40, and 50 mm/min tool traveling speeds are shown in Figure 3.

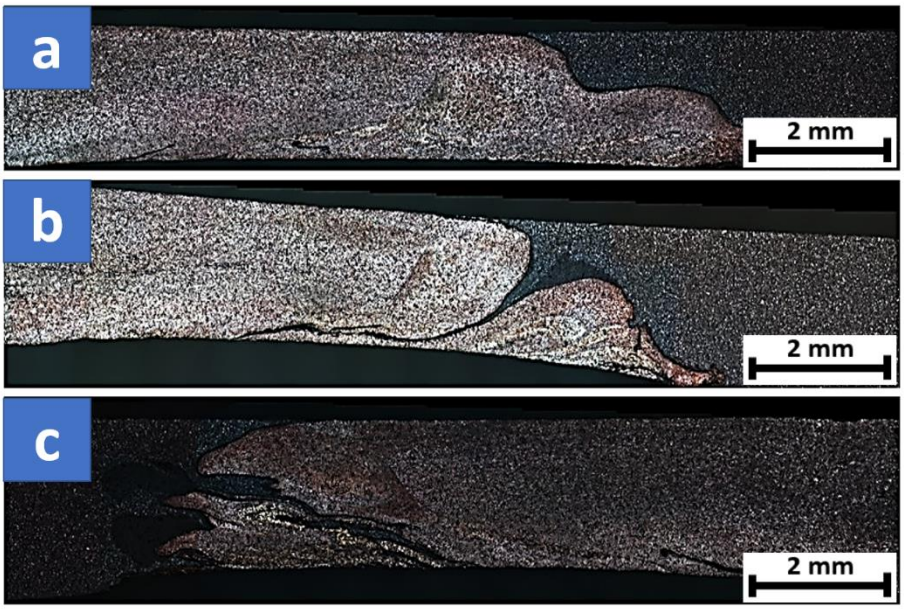

Figure 3. Macrostructure of full-welded zones of 0.95 Mg-Al-alloys and pure copper samples prepared by (a) 30, (b) 40, and (c) 50 mm/min tool travel speeds.

Figure 3 shows the macro view of three particular samples prepared at a constant tool rotational speed and varying tool travel speed of 30, 40, and 50 mm/min. As shown in the cross-sectional region, the intermixing of the weld region indicates strong bonding between aluminum and copper. The material flows directionally because of the threaded pin profiles.

The macroscopic aspect of the fabricated welds are shown in Figure 4. Better intermixing of the aluminum-copper joint was observed at 40 mm/min, depending on the tool rotational speed and traverse speed. Additionally, the other tool travel speeds produced better surface morphology. All three welded plates were without surface defects as shown in Figure 2. The macroscopic image of the weld zone showed no weld defects and the microstructural steadiness was observed. There were microstructural dissimilarities with sites relative to the unaffected base metal. The weld area exhibited numerous microstructurally distinct regions, including the DXZ zone along the weld centerline, and the heat-affected zone (HAZ) adjacent to the stir zone, as shown in Figure 4.

The base metal showed large deformation twins and slightly extended grain structures. However, the extended grain structure vanished near the weld zone. The increase in the grain size was because of the annealing effect of the welding heat. A very fine and equalized grain structure was observed in the mid region of the weld zone. The plastic shear deformation and frictional heat generated may have simultaneously caused the recrystallization.

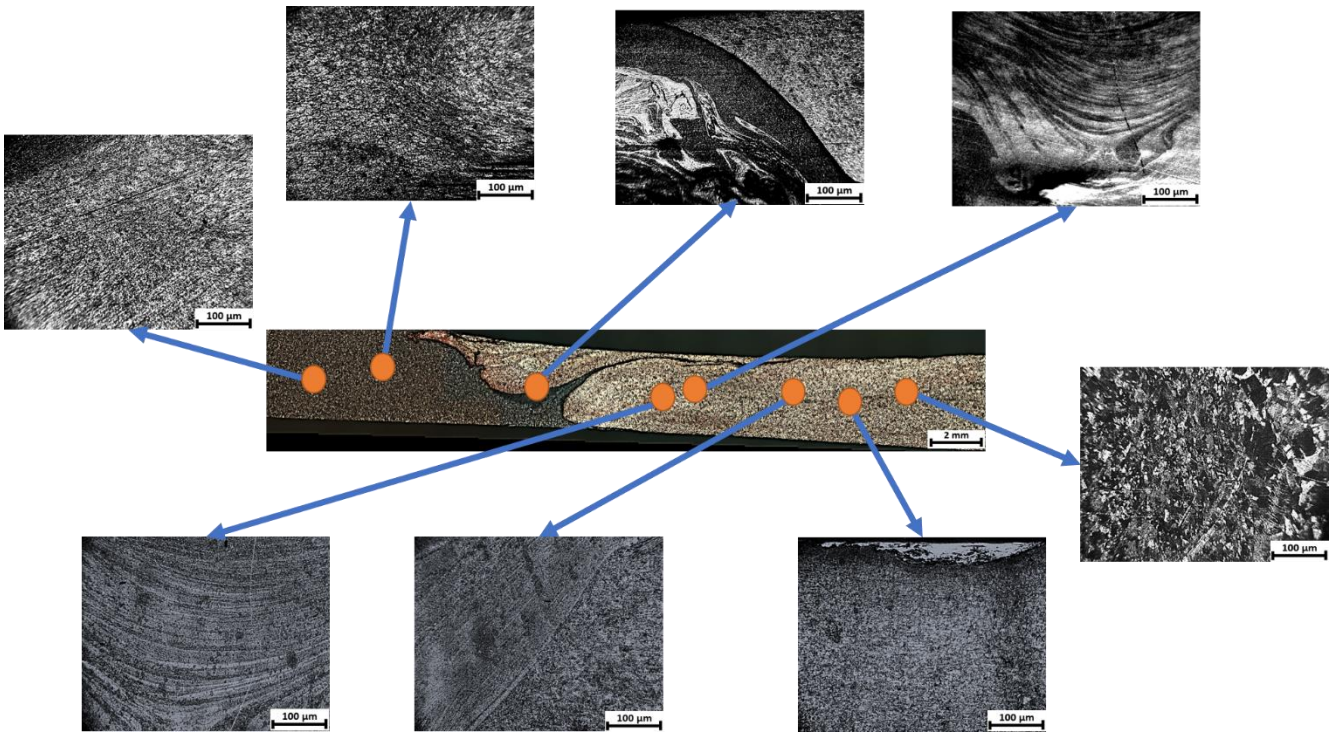

Figure 4. Microstructure view of different zones of the aluminum-copper welded sample using 1350 rpm and 40 mm/min process parameters.

3.2. Micrography Observation

The microscopic examinations suggests that the process parameters have a major impact on the formation of dissimilar aluminum-copper joints. Figure 4 shows the three different zones: the first is the heat affected zone (HAZ), the second is the thermo-mechanical affected zone (TMAZ), and the third one is the dynamic recrystallization zone (DXZ) or intermediate zone (IZ). The weldment is divided into two different sides, the advancing side (AS) and retreating side (RS). In this study, Cu is located at the advancing side and Al is located at the retreating side. The microstructure of the joints fabricated by a TT tool pin profile was studied using optical microscopy to expose the quality of the stir zone. The microstructure of the samples with a tool traverse speed of 40 mm/min led to the development of coarser grains. This may confirm greater heat contribution due to lower welding speeds that affects the coarsening of the grain size. The microstructure formed at a faster traverse speed of 50 mm/min had larger grains due to lower heat generation causing inadequate metal transportation, resulting in poor merging of the stirred materials. The microstructure at the faster tool travel speed of 50 mm/min exposed a mixture of coarse and fine grains.

The joints prepared by the tool rotation speed of 1350 rpm and weld speed of 40 mm/min produced joints without defects and with higher hardness, which may be attributed to the presence of smaller grains in the stir zone similar to other conditions. The observed intense plastic deformation and frictional heat generation was due to the faster tool rotation speed and welding speed. FSW produced homogeneous grains with finer structure that might have caused the enhancement in the properties.

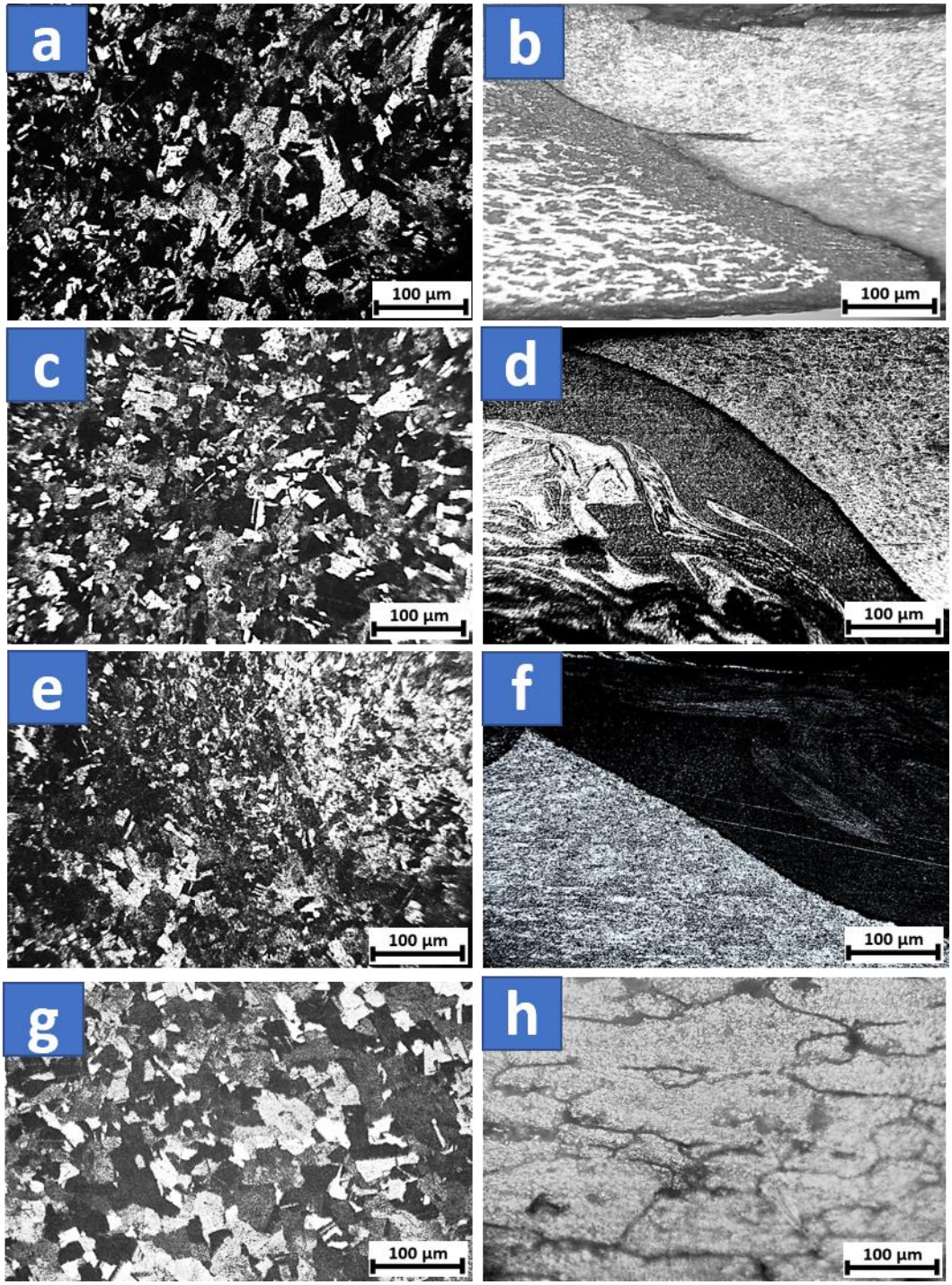

Figure 5. Microstructure view after and before welding of pure copper (left side) and 0.95 Mg-Al alloy (right side) using (a-b) 30, (c-d) 40, and (e-f) 50 mm/min tool travel speeds. (g-h) The BM alloy.

The enlarged boundary between the Al matrix and Cu bulk is shown in Figure 4. The microstructure with full view of the weldment and differentzones such as heat affected zone (HAZ), thermomechanical affected zone (TMAZ), and dynamic recrystallization zone (DXZ), which is also known as the stir zone, were observed in Figure 4. During welding, dynamic recrystallization occurred in the complete welding zone because of sufficient heat generation and suitable parameters with the

threaded tool pin profile. The material directional flowability and aluminum-copper joint are both face center cubic (FCC) materials, soft but with different melting points. If the solidification time is longer or the surface is uneven, $CuAl_2$, CuAl, and Cu_9Al_4 can form. These are intermetallic phases that cause defect formation due to Cu_9Al_4, which is very brittle, and Cu_9Al_4 is formed in the 350 – 410°C temperature range [16].

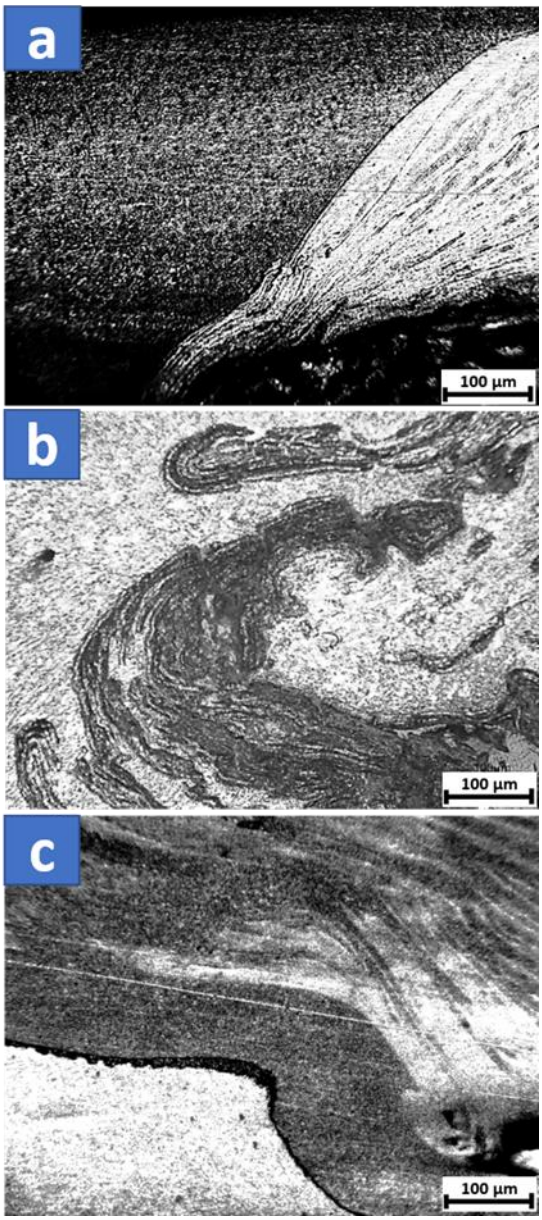

Figure 6. Microstructure of the stir zone (SZ) of aluminum-copper FSW joints prepared at (a) 30, (c) 40 and (e) 50 mm/min tool travel speeds.

The faster and slower tool traverse speeds indicate better deformations because of sufficient heat generation [17]. As shown in Figure 5a-b, the aluminum-copper joint at 30 mm/min had a slight deformation in the grain size. In the case of the 50 mm/min tool travel speed, the deformation is much

less due to the lack of heat generation as shown in Figure 5e-f. However, 40 mm/min produced the best deformation due to sufficient heat generation and proper fusion of aluminum and copper metals that are evident in Figure 5c-d. Reduction of the grain size and intermixing of aluminum-copper are better than a faster tool travel speed for weld fusion of aluminum-copper. The absence of a deformed BM microstructure is an indication of microstructural significance, as shown in Figure 5g-h [18].

The image of the interface between Al and Cu is presented in Figure 6. The interface region of the FSW prepared with a 30 mm/min tool travel speed is shown in Figure 6a, 40 mm/min is shown in Figure 6b and 50 mm/min is shown in Figure 6c. The Cu material adjacent to the area of the interface was plasticized due to optimal heat. Therefore, the fine intermittent Cu particles were separated and dispersed in the stir region. An interface exists between the Al matrix and Cu bulk, which is evident by the layered structure detected in the Cu bulk at the aluminum-copper interface.

3.3. Microhardness examination

The mechanical properties of the FSW joints prepared 30, 40, and 50 mm/min tool travel speeds are shown in Figure 7. The joint prepared by the TT pin profile experienced superior properties with the joint efficiency of 78% compared to the other joints. The TT pin profile sweeps large amount of material from the plasticized zone [19]. The joint fabricated by the 30 mm/min tool travel speed shows less hardness than the joint prepared at 40 mm/min tool travel speed. The friction heat generated by 30 mm/min tool travel speed may be less than that by 40 mm/min tool travel speed because the uneven heat generation and solidification of the weldment of the aluminum-copper joint is not suitable, and the formation of the intermetallic compounds and pin exerts an extra downward force. This fine grain structure resulted in a more ductile nature than all other joints. The microhardness that resulted from the 50 mm/min tool travel speed are slightly less than the 40 mm/min tool travel speed. The increase in heat generation and the creation of additional intermetallic compounds at the aluminum-copper interface resulted in grains slightly larger than the 40 mm/min tool travel speed. A clear nugget zone was observed, which differs from the 30 mm/min specimen with low hardness. Moreover, the homogenous dissemination of Cu bulk in Al increases the mechanical properties of the 40 mm/min specimen. A previous microhardness survey on all the welded joints was demonstrated by different tool travel speeds [20]. The microhardness values equate to lesser BM in different conditions using different tool travel speeds, as shown in Figure 7. The improved hardness of the joint is less than the specific parameter conditions of the 40 mm/min tool travel speed and TT (tool pin profile).

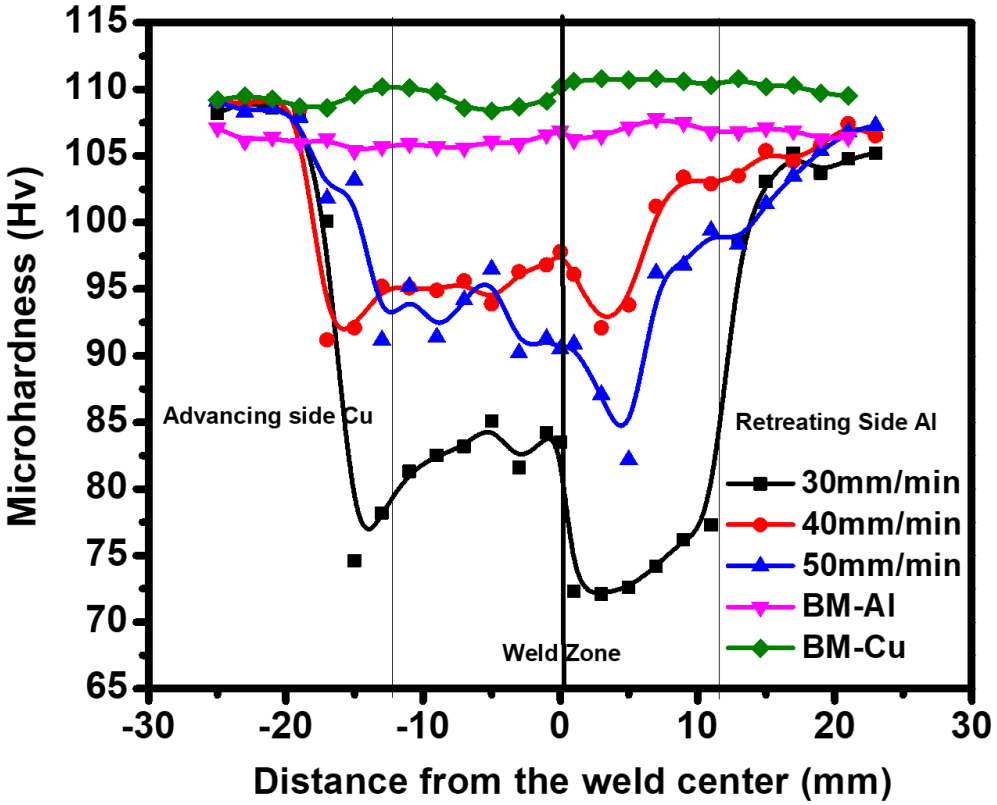

Figure 7. Microhardness distribution in the FSW joints for different tool travel speeds. The base metal (aluminum-copper) advance side is copper and the retreating side is aluminum.

3.4. Results obtained prior to the corrosion tests

Figure 2 shows the XRD patterns for the three samples with BMs. The peaks of the base alloy with different travel speeds, such as 30 and 50 mm/min, were identified as Cu_9Al_4, Al_2Cu, Al, and Cu. The stirring behavior at the weld center and finer grains were observed [1, 6].

The stirring of the tool persuades significant plastic deformation and frictional heat generation between the tool and BM, which is due to the presence of constant dynamic recrystallization zone (DXZ) [21]. The DXZ typically occurs in the weld zone, and thus the microstructures can be refined. Small portions of TMAZ and HAZ were seen between the WZ and BM zone. A slightly elongated grain structure is observed in the TMAZ zone due to severe plastic deformation and the annealing effect of heat on the material near the pin verge [22]. Slightly coarse grains were observed in the HAZ zone outside of the TMA-zone, which was altered only by the heat formed during the welding procedure [23]. DXZ is important for industrial applications as it shows the new grains that are smaller than the initial grains that enhances the mechanical parameters at room temperature.

3.5. Scanning electron microscopy (SEM) examination after the corrosion test

Previous research has established that intermittent particles affect the corrosion of Al alloys [24-27]. The shape of the intermetallic elements (i.e., spheroids, fiber-like or plate-like) is intensely altered by the applied cooling rate throughout solidification [28, 29]. The segregation of the intermetallic

particles, such as Al_4Cu_9 and Al_2Cu, cause the cracks and pits in the WNZ and HAZ regions. Figure 8a shows a film formed due to corrosion products with small cracks that are quite heterogeneous as the formation of the cracks causes brittleness, affecting the generation of the intermixing zone cracks. These cracks might be correlated to the intergranular corrosion in the base alloy subsequent to the corrosion reaction.

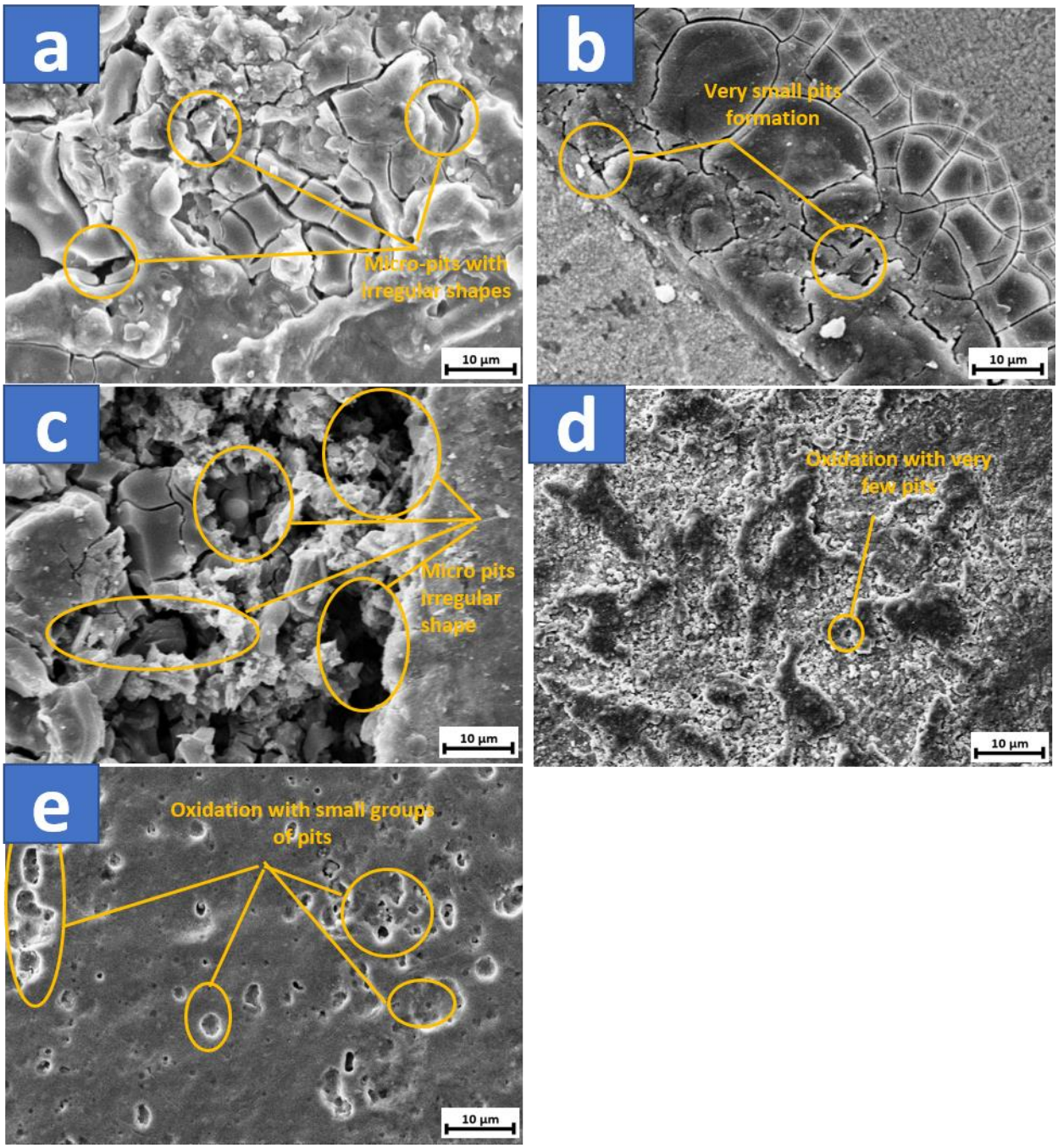

Figure 8. SEM analysis after electrochemical tests showing micro pits on the exposed area of the (a) 30 mm/min tool travel speed, (b) 40 mm/min tool travel speed, (c) 50 mm/min tool travel speed, (d) pure copper and (e) 0.95 Mg-Al-Alloy samples.

The HAZ region in the weld zone undergoes intense pitting corrosion compared to the base alloy for FSW. Several minor intergranular outbreaks are connected with the rusted surface of HAZ. As shown in Figure 8b, samples prepared at the 40 mm/min tool travel speed showed no pit formation because of the better corrosion resistance of the joints. The figure shows the oxide layer during corrosion that is not as severe as the grain boundary cracking or pits formation. Figure 8c shows the surface of the sample welded at a 50 mm/min tool travel speed with irregular pits and rough surface. The generation of micropits on the welded surface and grain boundary cracking were observed after electrochemical tests on the BM alloy as shown in Figure 8d-e. Pitting is observed on the surface of BMs due to the corrosive media. The cathodic route at the component element induces alkalization [30, 31] that causes the dissolution of the Al matrix, which may also contribute to the porous nature of the surface layer.

As shown in Figure 7c, the corrosion properties for the joint prepared with the 50 mm/min tool travel speed were slightly better than joints prepared at 40 mm/min. The increase in the heat generation and the generation of more intermittent elements at the aluminum-copper boundary enhanced brittleness and reduced the tensile strength. As previously mentioned in [32], the lower tensile strength of the joint is due to the increase in the thickness of the intermetallic segments.

3.6. Phase analysis of the aluminum-copper welded samples after the electrochemical tests

The XRD pattern of aluminum-copper illustrates the peak shift of the Al and Cu metals [33]. The identified intermetallic formation on the interface region from such compounds as Cu_9Al_4 and $CuAl_2$ were observed in the aluminum-copper weldment samples.

The X present phases and phases during welding of the intermetallic can also be detected by XRD analysis. 0.95 Mg-Al-alloy and pure copper specimens were welded using different tool travel speeds. The peaks of the base metals and interface regions of weldment at different tool travel speeds of (a) 0.95 Mg-Al-alloy (b) Pure Copper (c) 30 mm/min (d) 40 mm/min (e) 50 mm/min are shown in Figure 9. The XRD results clarified the present phases or phases formed during welding. Some specific intermetallic phases were formed, such as CuAl, $CuAl_2$, and Cu_9Al_4, and a remaining amount of α-Al and Cu was also observed.

The present phases demonstrate that the weld of the 0.95 Mg-Al-alloy to pure Cu involves the intermetallic compound, such as $CuAl_2$, CuAl, and Cu_9Al_4, composed with some of the α-Al and Cu. The single phases of α-Al and copper were identified near the 0.95 Mg-Al-alloy and near the leading intermetallic compounds as exposed in Figure 9c. No discrete α-Al peak was detected and intermetallic compound peaks correlate with the complex mixing of 0.95 Mg-Al-alloy and pure Cu grains in the weld zone. As shown in Figure 9d, at a tool travel speed of 40 mm/min, there were no intermetallics because of the sufficient heat generation and proper bonding between aluminum-copper.

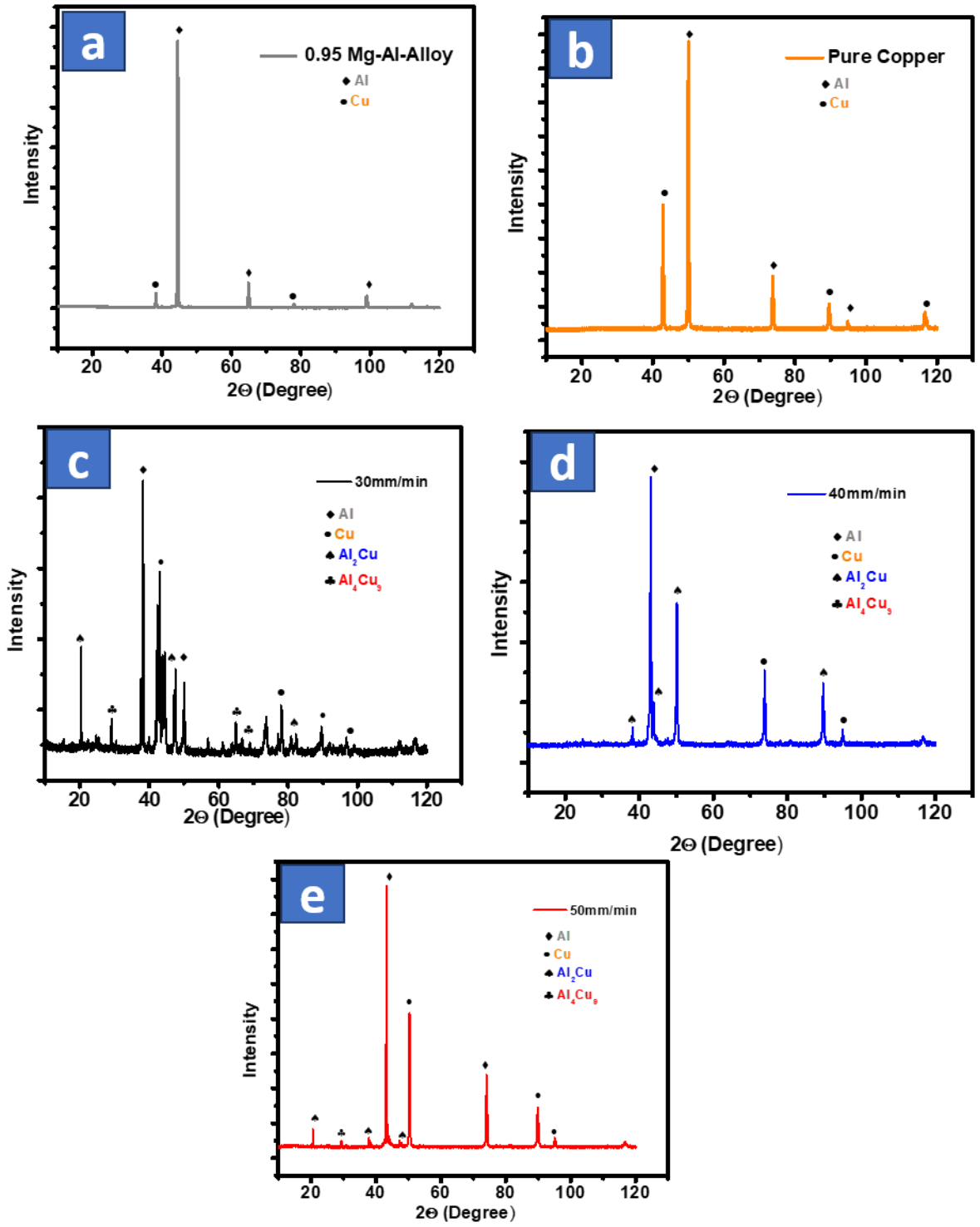

Figure 9. XRD plots showing the peaks of the base metals and interface region of the weldment at different process parameters: (a) 0.95 Mg-Al-alloy, (b) pure copper, (c) 30 mm/min tool travel speed, (d) 40 mm/min tool travel speed and (e) 50 mm/min tool travel speed samples.

The XRD results showed that the high temperatures related with the strong stirring movement tool travel speed at 50 mm/min in Figure 9e cause the heterogeneous involvement of Al and Cu and the formation of intermetallic compounds of $CuAl_2$, CuAl, and Cu_9Al_4. The peaks of the FCC structure of

copper with varied configurations of aluminum mostly detached at the bottom of the weld as shown in Figure 9. The ratios of the aluminum and copper composition vary by 18.4 wt. % in the single phase Cu.

The high temperature related to the robust stirring action tool travel speed results in the nonuniform mixing of the aluminum-copper joint at 50 mm/min and causes the creation of intermetallic compounds CuAl, $CuAl_2$, and Cu_9Al_4 [34].

A diverse deposition of aluminum and copper containing $CuAl_2$, CuAl, and Cu_9Al_4 are detected through the XRD analysis and microstructural interpretations in a dissimilar weld [35]. Therefore, the softening of the stirred 0.95 Mg-Al-alloy allows the development of a diverse layer and intermetallic compounds.

3.7. Potentiodynamic polarization studies

Polarization studies are globally used to observe the rate of corrosion for a metal or alloy in contact with a corrosive media. Tafel plots were documented with in a range of -250 mV to +250 mV at a scan rate of 1 mV/s. The results were further quantitatively examined to obtain the Tafel slopes (β_a and $-\beta_c$), the corrosion potentials ($-E_{corr}$) and corrosion current density (I_{cor}). The anodic current density (I_a) can be stated by the following equations:

$$I_{reaction} = I_a = -I_o \exp(1-\beta \frac{nF}{RT}\eta_{reaction}) \quad (1)$$

$$\eta_a = b_a \log_{10}(\frac{I_a}{I_o}) \quad (2)$$

$$b_a = 2.303\frac{RT}{\beta nF} \quad (3)$$

Or, $b_c = -(\beta nF / RT)$ and $b_a = [(1-\beta)nF / RT]$

where the number of electrons (n) for an unidentified reaction can be obtained. The experiments were conducted in 3.5 wt % NaCl solution. The results are shown in Table 3.

Table 3. Aluminum-copper in 3.5 wt% NaCl for different conditions and a constant tool pin profile.

Sample Condition	Cathodic β(mV)	Anodic β(mV)	E_{corr} (mV)	I_{corr}(μA)
BM/Copper	318	93	-215	16
BM/Aluminum	630	30	-645	11
30 mm/min	476	25	-639	18
40 mm/min	470	55	-578	15
50 mm/min	637	34	-657	24

Figure 10 shows the polarization potentiodynamic graph of the three examined tool travel speeds of 30 mm/min, 40 mm/min, and 50 mm/min samples in a stationary and aerated 3.5% NaCl solution at 22 (±2) °C.

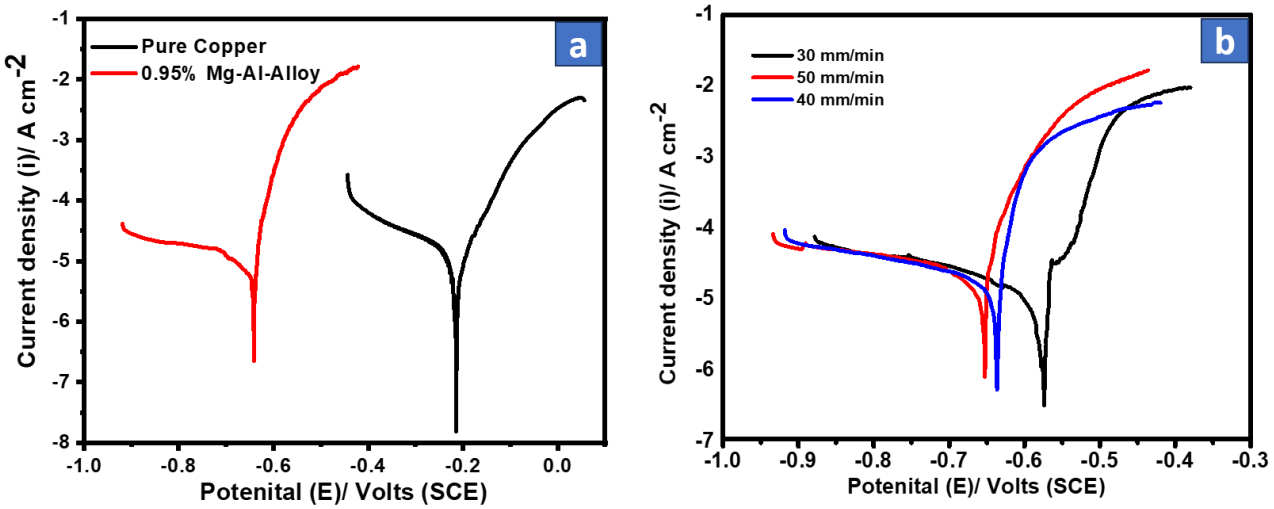

Figure 10. Polarization graphs of samples in 3.5 wt. % NaCl solution at 22 ± 0.5 °C for the (a) base metals and (b) welded samples prepared at tool travel speeds of 30, 50, and 40 mm/min.

Based on the three potentiodynamic polarization curves, the Al–Cu alloy displays corrosion of the Cu-rich phase and formation of copper oxide. This possibly initiates the mechanism of precipitation and dissolution of $AlCl_2$, Cu(OH)4, CuO, and MgO corrosion products. Regarding the Al–Cu alloy sample, a partial steadiness was detected in the current density value of 10.892 µA cm^{-2}. Notably, the formation of copper oxide becomes more stable near -578 mV (SCE) [36]. Both anodic and cathodic shifts can be observed in the potentiodynamic curves. The samples prepared with a tool travel speed of 40 mm/min showed the best performance with a lower corrosion current density rate of 14.776 µA cm^{-2} followed by 30 mm/min with 18.205 µA cm^{-2} and 50 mm/min with 24.232 µA cm^{-2}. As shown in Table 3, BM aluminum showed less corrosion current density than the samples prepared with a 40 mm/min tool travel speed [37]. The current range was used to avoid the overloading of the instrument during the hot corrosion process at the tool travel speeds.

3.8. Electrochemical impedance

After immersion of the welded samples in 3.5 wt.% NaCl solution, Nyquist, Bode and phase angle plots were obtained, as shown in Figure 11. The impedance and phase angle increased with an increase in the FSW tool travel speed. The values of the various parameters after fitting the corresponding circuit are shown in the Table 4. R_s is the solution resistance, R_{ct} is the charge transfer resistance, and CPE is a constant phase element in the equivalent circuit.

$$Z_{CPE} = R_s + \frac{R_{ct}}{1 + R_{ct} Y (j\omega)^n} \quad (4)$$

$$\left((j\omega)^n = \omega^n e^{j\frac{n\pi}{2}} = \omega^n \left(\cos\frac{n\pi}{2} + j \sin\frac{n\pi}{2}\right) \right) \quad (5)$$

We can obtain the equation below after interpretation:

$$\left(Z`-R_s-\frac{R_{ct}}{2}\right)^2+\left(-Z^n+R_{ct}\cot\frac{n\pi}{2}\right)^2=\left(\frac{Rct}{2}\csc\frac{n\pi}{2}\right)^2 \quad 6)$$

The depressed semicircle is represented by the above equation. The Z_{CPE} of a CPE is conveyed as

$$Z_{CPE}=\frac{1}{Y_o}[(j\ X\ 2\pi f_{max})_n]^{-1} \quad 7)$$

where Y_o is the amplitude, j is the square root of −1, f_{max} is the AC frequency and n is the phase shift. When n = 0, the CPE signifies a pure resistor, if n = +1, then the CPE is characterized as a pure capacitor; if n = −1, then CPE denotes an inductor [38].

Figure 11a displays the fit result of the Nyquist plot with equivalent circuit and frequencies. Figure 11b shows the Nyquist plots of pure copper and 0.95% Mg-Al alloy BMs in a NaCl solution. Figure 11c displays the Nyquist plots of the welded samples with different tool travel speeds of 30 mm/min, 40 mm/min, and 50 mm/min after exposure to the corrosive media. A depressed semicircle can be observed for all samples suggesting that the overall mechanism is not modified.

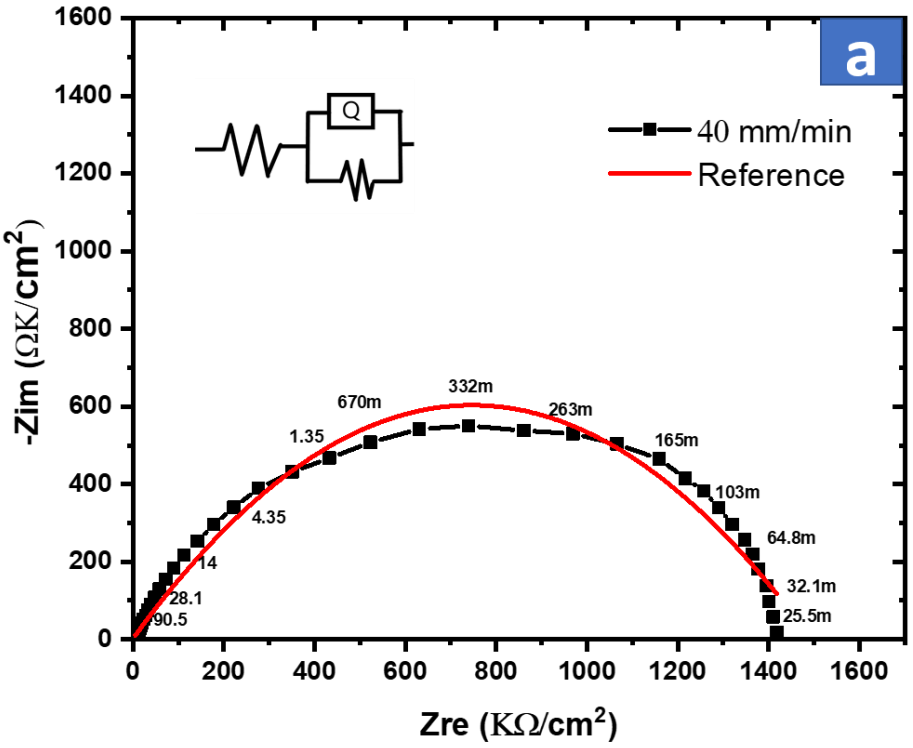

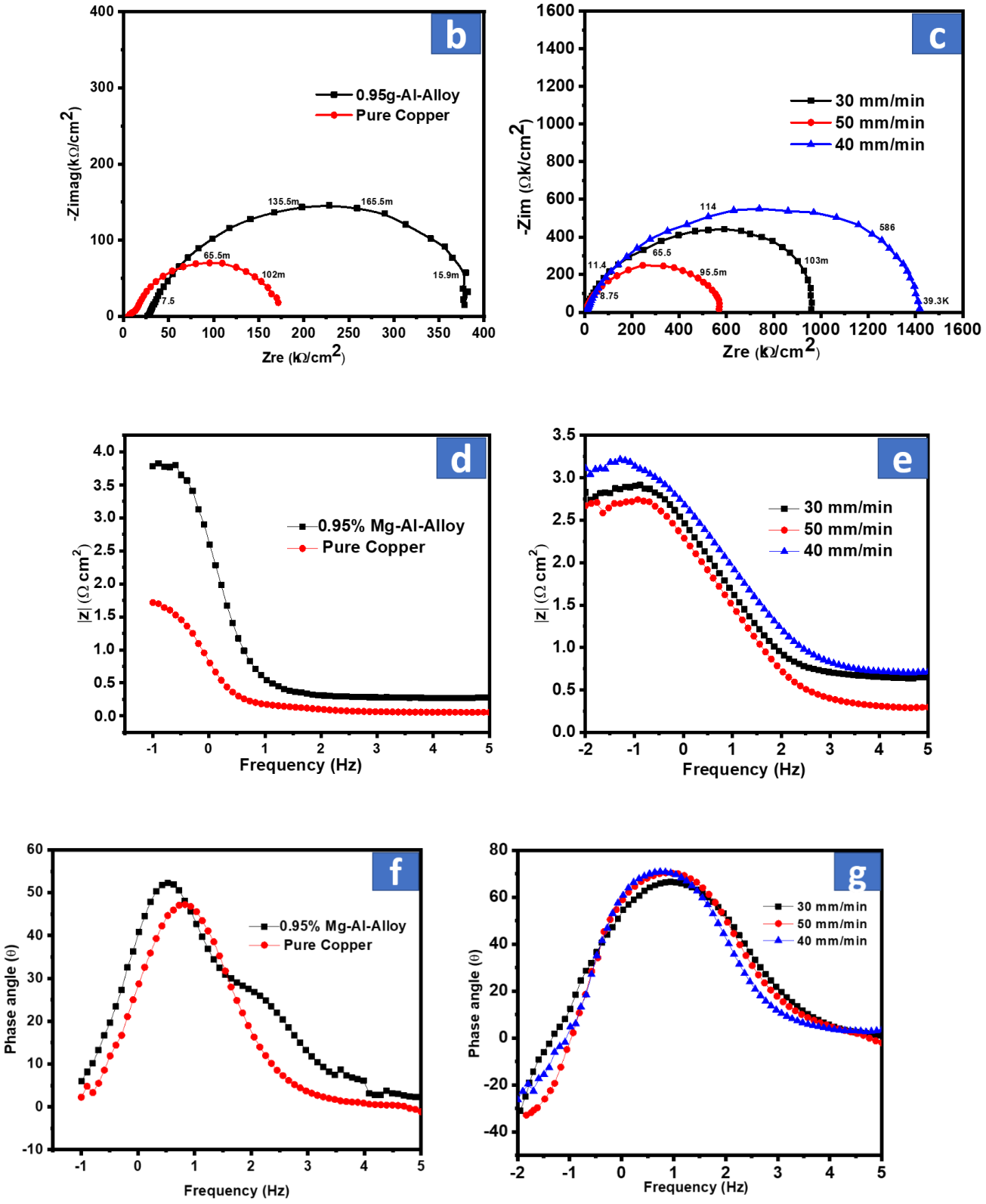

Figure 11. Electrochemical spectra of samples with and without deformation. (a) Fit results of the Nyquist plot with frequency and equivalent circuit used. (b-c) Nyquist, (d-e) Bode and (f-g) phase angle plots.

Table 4. Impedance data for aluminum-copper in 3.5 wt. % NaCl at various tool travel speeds.

Samples	R_s (ohm cm^2)	CPE S.sn.cm^{-2}	n	R_{ct} (ohm cm^2)	-*S*	α (°)
0.95 Mg-Al-alloy	28	0.0004	0.8	376	0.9	52
Copper	5	0.0010	0.7	179	0.9	47
30 mm/min	5	0.0006	0.9	986	0.8	64
40 mm/min	3	0.0010	0.8	1412	0.9	64
50 mm/min	5	0.0004	0.8	573	0.7	61

The corrosion resistance was the best for the sample welded with the 40 mm/min tool travel speed. The width of the Nyquist plots increased with an increase in the charge transfer resistance (R_{ct}) as expressed in Table 4. The best resistance was shown at 1412 kΩ cm^2 followed by 986 kΩ cm^2 and 573 kΩ cm^2, respectively.

Figure 11d shows the Bode plots of pure copper and 0.95% Mg-Al alloy BMs in the corrosive solution. Figure 11e shows the Bode plots of the samples welded with different tool travel speeds of 30 mm/min, 40 mm/min and 50 mm/mins. The slope values obtained from the intermediate frequencies show that as the corrosion resistance increases, the value tends to move closer to 1. The closest value was obtained for a 40 mm/min tool travel speed welded sample with 0.866, 0.820 for the 30 mm/min welded sample and 0.744 for the 50 mm/min welded sample as represented in Table 4.

Figure 11f shows the phase-angle plots of pure copper and 0.95% Mg-Al alloy BMs in the NaCl solution. Figure 11g shows the phase-angle plots for the welded samples in different frequency ranges. The phase angle plots move closer to a 90° angle for a good corrosion resistant surface. The best angle was observed at 64.2°, approaching 90° for the 40 mm/min tool travel speed. This result was followed by 63.9° for the 30 mm/min welded sample and 61.3° for welded sample prepared at the 50 mm/min tool travel speed as shown in Table 4.

3.9. Scanning Kelvin probe (SKP)

SKP is one the most sophisticated methods available to perceive the confined corrosion on the metal surface. The probe vibrates over the working electrode surface creating a capacitor and an alternating current that flows between the probe and the working electrode [39]. Figure 12a represents the aluminum sample before corrosion and 12b represents and after corrosion. As shown in Figures 12a and 12b, the anodic activity was grater after corrosion. The anodic potential is distributed all over the surface due to corrosion and the formation of pits. A similar case was observed for the copper sample as shown in Figure 12c and 12d. The corrosive media attacked the surface, and as a result, the anodic potential dominates. Figure 12e and 12f represents the sample welded at a 40 mm/min tool travel speed before and after corrosion. As shown in Figure 12e, the sample is distinguished as aluminum, copper and intermetallic (welded) zones. This distinguished zone disappears as the corrosive solution attacks the surface leading to roughness, cracks and pits. More anodic potential was observed in the case of

corrosion or pit formation while the cathodic potential was observed prior to corrosion suggesting that the surface was still intact and not corroded. These results support the EIS and Tafel results.

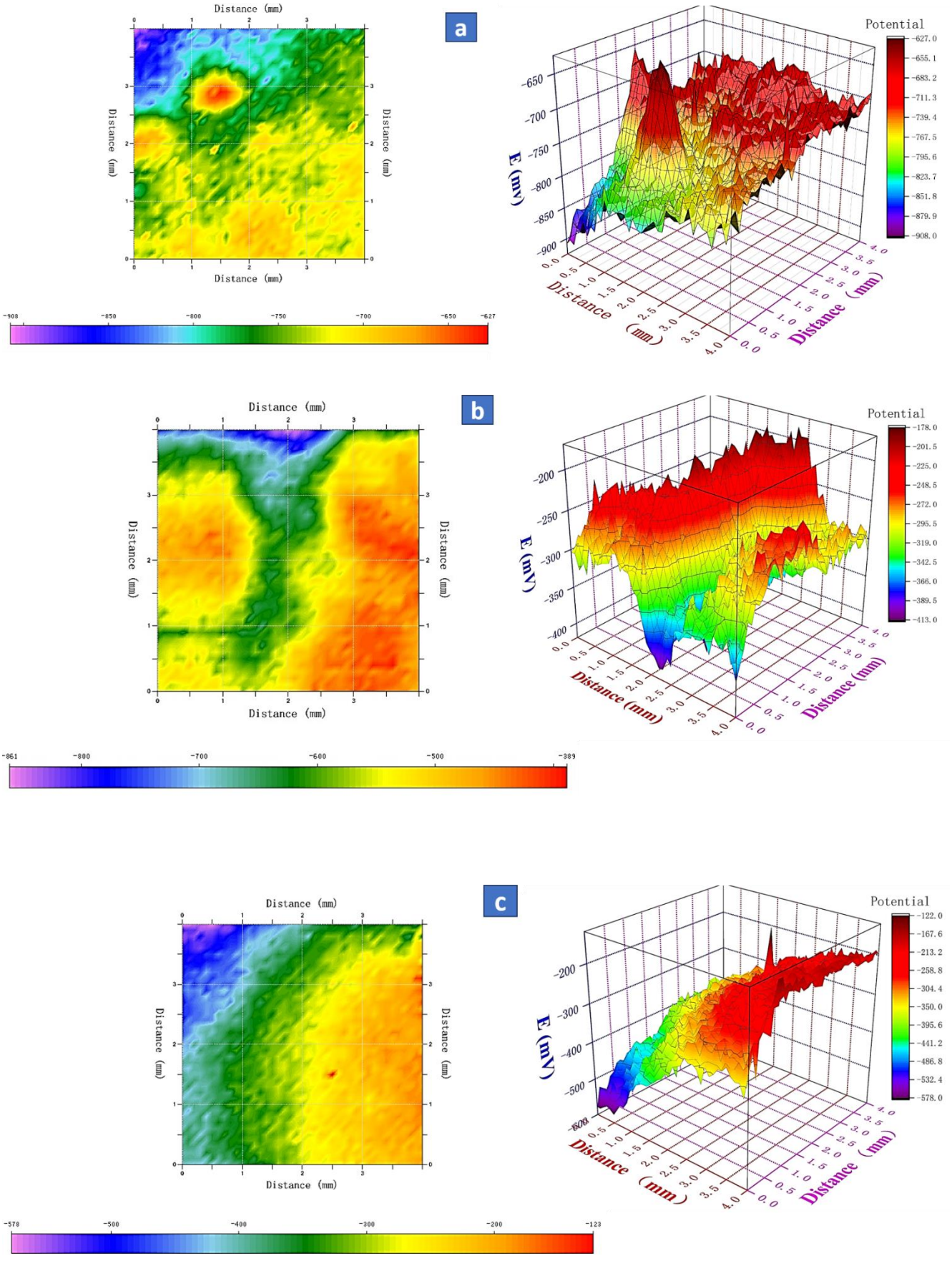

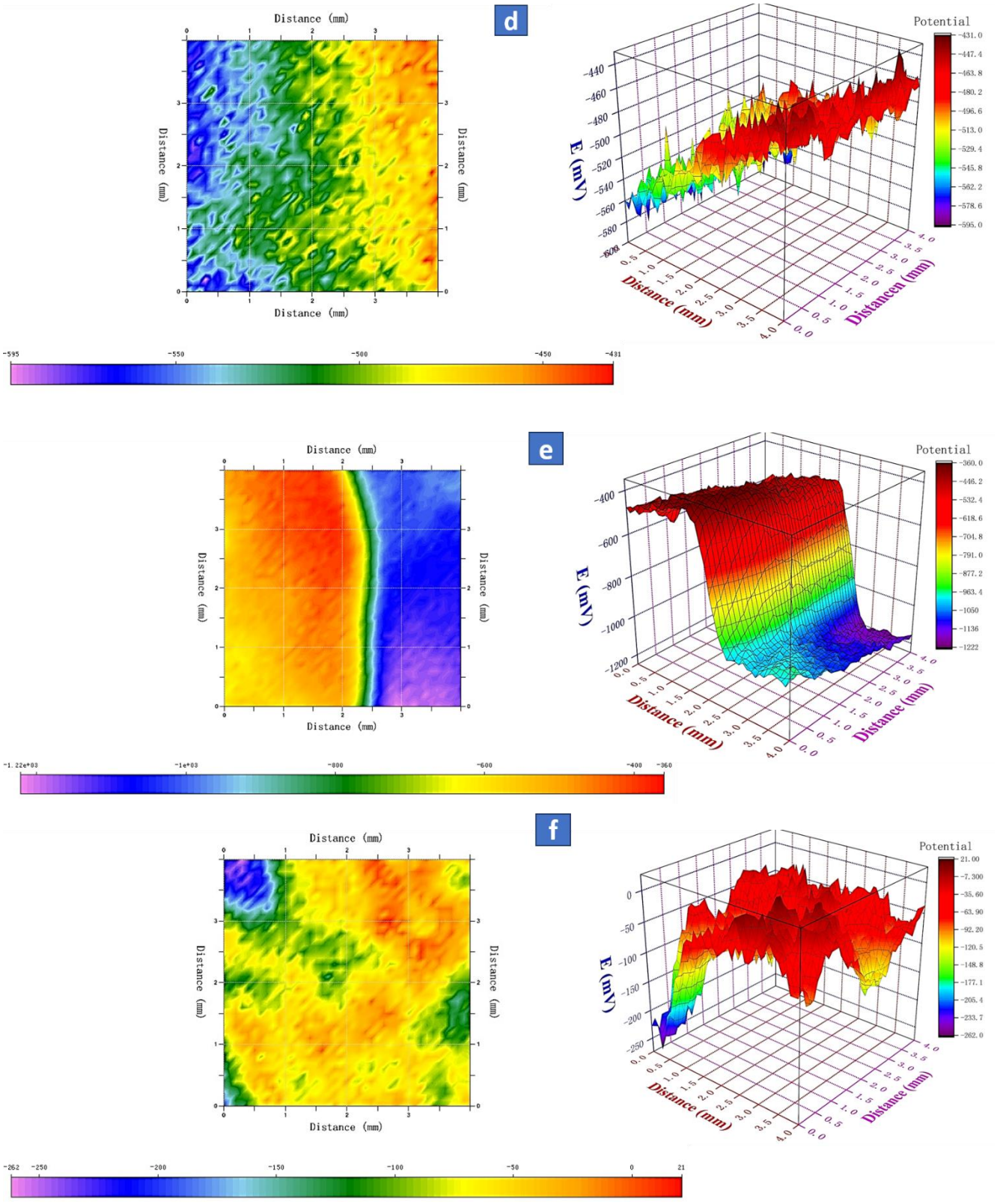

Figure 12. SKP spectra of samples before and after corrosion. (a) 2D and 3D images of pure Al, (b) pure Al after corrosion, (c) pure Cu, (d) pure Cu after corrosion, (e) a sample welded at 40 mm/min and (f) a sample welded at 40 mm/min after corrosion.

4. CONCLUSIONS

(1) Three different tool travel speeds of 30, 40 and 50 mm/min were used for friction stir welding of 0.95 Mg-Al-alloy and pure Cu specimens; 40 mm/min was found to be the most suitable tool travel speed for a Cu-Al dissimilar defect-free joint.

(2) SEM and XRD analyses demonstrated that the change in the grain size from elongated to small was mainly caused by increasing the FSW tool travel speed.

(3) The polarization showed a shift in both the anodic and cathodic regions. The corrosion current density was lowest for the 40 mm/min welded samples, suggesting good corrosion resistance in the presence of a corrosive solution.

(4) Electrochemical impedance suggested that the corrosion resistance of the welded sample prepared with a 40 mm/min tool travel speed was the best in 3.5 wt.% NaCl solution.

ACKNOWLEDGEMENTS
The authors are thankful to the Sichuan 1000 Talent Fund, financial assistance provided by the Youth Scientific and Innovation Research Team for Advanced Surface Functional Materials, Southwest Petroleum University number-2018CXTD06 and open fund project number-X151517KCL42.

References

1. W. M. Thomas, E. D. Nicholas, J. C. Needham, M. G. Murch, S. P. Temple, C. J. Dawes, Improvements relating to friction stir welding. (1991) G.B. Patent No.9125978.8.
2. S. W. Stratton, Copper wire tables, 13th edition, Washington, (1914).
3. N. D. Nam, L. T. Dai, M. Mathesh, M. Z. Bian, V. T. H. Thu, *Mater. Chem. Phys*. 3 (2016) 7.
4. F. A. Ghauri, K. M. Deen, A. Farooq, M. Afzal, A. Ahmad, *JMEPEG*. 27 (2018) 3429.
5. Gharavi Farhad, Amin Matoria Khamirul, Yunus Robiah, Kamil Othman Norinsan, Fadaeifard Firouz, *J. Mater. Res. Technol*. 4 (2015) 314.
6. J. Ouyang, E. Y. Reddy, R. Kovacevic, *J. Mater. Process. Technol*. 172 (2006) 110.
7. Celik Sare, Cakir Recep, *Metals* 6 (2016) 133.
8. P. Staron, M. Kocak, S. Williams, A. Wescott, *Phys. B*. 350 (2004) 491.
9. O. Hatamleh, I. V. Rivero, A. Maredia, *Metall. Mater. Trans*. A. 39 (2008) 2867.
10. V. Farajkhah, Y. Liu, *Int. J. Adv. Manuf. Technol*. 90 (2017) 339.
11. D. Wadeson, X. Zhou, G. Thompson, P. Skeldon, L. D. Oosterkamp, and G. Scamans, *Corros. Sci*. 48 (2006) 887.
12. J. Kang, R. D. Fu, G. H. Luan, C. L. Dong, M. He, *Corros. Sci*. 52 (2010) 620.
13. M. Jariyaboon, A. Davenport, R. Ambat, B. Connolly, S. Williams, D. Price, *Corros. Sci*. 49 (2007) 877.
14. K. Surekha, B.Murty, K. P. Rao, *Solid State Sci*. 11 (2009) 907.
15. W. Xu, J. Liu, H. Zhu, *Electrochim. Acta*. 55 (2010) 2918.
16. N. Birbilis, R. G. Buchheit, *J. Electrochem. Soc*. 155 (2008) 117.
17. M. Jafarzadegan, A. H. Feng, A. Abdollah-zadeh, T. Saeid, J. Shen, and H. Assadi, *Mater. Charact*. 74 (2012) 28.
18. M. V. Suresh, B. Vamshi Krishna; P. Rao, *Sci Technol Weld Joi*. 9 (2004) 362.
19. D. M. Rodrigues, A. Loureiro, C. Leitao, R. M. Leal, B. M. Chaparro, P. Vilaça, *Mater. Des*. 30 (2009) 1913.

20. A. Kumar, L. S. Raju, *Mater. Manuf. Process*. 27 (2012) 1414.
21. C. V. Rao, G. M. Reddy, K. S. Rao, *Def. Technol*. 11 (2015) 123.
22. A. Devaraju, *Mater. Today Proc*. 4 (2017) 3722.
23. Gharavi Farhad, Amin Matori Khamirul, Yunus Robiah, Kamil Othman Norinsan, *Mat. Res.* 17 (2014) 1563.
24. F. Zucchi, G. Trabanelli, V. Grassi, *Mater. Corros*. 52 (2001) 853.
25. M. Trueba, S. P. Trasatti, *Mater. Chem. Phys*. 121 (2010) 523.
26. B. Zaid, D. Saidi, A. Benzaid, S. Hadji, *Corros. Sci.* 50 (2008) 1841.
27. W. R. Osorio, L. R. Garcia, L. C. Peixoto, A. Garcia, *Mater. Des*. 32 (2011) 4763.
28. W. R. Osorio, C. M. Freire, R. Caram, A. Garcia, *Electrochim. Acta*. 77 (2012) 189.
29. H. Ezuber, El. A. Houd, El. F. Shawesh, *Mater. Des*. 29 (2008) 801.
30. J. O. Park, C. H. Paik, Y. H. Huang, R. C. Alkire, *J Electro. Chem. Soc.* 146 (1999) 517.
31. D. M. Rodrigues, A. Loureiro, C. Leitao, R. M. Leal, B. M. Chaparro, P. Vilaça, *Mater. Des*. 30 (2009) 1913.
32. V. Aditya Ayyagari, Bharat Gwalani, Saideep Muskeri, Sundeep Mukherjee, Rajarshi Banerjee, *Mater. Degrad*. 2 (2018) 1.
33. P. Xue, D. R. Ni, D. Wang, B. L. Xiao, Z. Y. Ma, *Mater. Sci. Eng*. C. 528 (2011) 4683.
34. A. Kumar, S. Sunderrajan, *Int. J. Adv. Manuf. Technol*. 42 (2008) 118.
35. M. V. Suresh, Krishna B. Vamshi, *Sci Technol Weld Joi*. 9 (2004) 362.
36. S. Rajkumar, C. Muralidharan, V. Balasubramanian, *Mater. Des*. 32 (2011) 535.
37. X. L. Zhang, Zh. H. Jiang, Zh. P. Yao, Y. Song, D. Zh. Wu, E *Corros. Sci*. 51 (2009) 581.
38. D. K. Yadav, M. A. Quraishi, *Ind. Eng. Chem. Res*. 51 (2012) 14966.
39. Feng Hongwei, Ambrish Singh, Wu Yuanpeng, Lin Yuanhua, *New. J. Chem*. 42 (2018) 11404.

© 2019 The Authors. Published by ESG (www.electrochemsci.org). This article is an open access article distributed under the terms and conditions of the Creative Commons Attribution license (http://creativecommons.org/licenses/by/4.0/).